This manuscript has been authored by UT-Battelle, LLC under Contract No. DE-AC05-000R22725 with the U.S. Department of Energy. The United States Government retains and the publisher, by accepting the article for publication, acknowledges that the United States Government retains a non-exclusive, paid-up, irrevocable, world-wide license to publish or reproduce the published form of this manuscript, or allow others to do so, for United States Government purposes. The Department of Energy will provide public access to these results of federally sponsored research in accordance with the DOE Public Access Plan (http://energy.gov/downloads/doe-public-access-plan).

Comparison of the thermal stability in equal-channel angular pressed and highpressure torsion processed Fe-21Cr-5Al alloy

Maalavan Arivu¹, Andrew Hoffman², Jiaqi Duan¹, Jonathan Poplawsky³, Xinchang Zhang⁴, Frank Liou⁴, Rinat Islamgaliev⁵, Ruslan Valiev⁵, Haiming Wen^{1,2,*}

¹Department of Materials Science and Engineering, Missouri University of Science and Technology, Rolla, MO 65409, USA

²Department of Nuclear Engineering and Radiation Science, Missouri University of Science and Technology, Rolla, MO 65409, USA

³Center for Nanophase Materials Science, Oak Ridge National Laboratory, Oak Ridge, TN 37830, USA

⁴Department of Mechanical and Aerospace Engineering, Missouri University of Science and Technology, Rolla, MO 65409, USA

⁵Institute of Physics of Advanced Materials, Ufa State Aviation Technical University, Ufa 450008, Russia

*Corresponding author: wenha@mst.edu

ABSTRACT

Nanostructured steels are expected to have enhanced irradiation tolerance and improved strength. However, they suffer from poor microstructural stability at elevated temperatures. In this study, Fe-21Cr-5Al-0.026C (wt.%) Kanthal D (KD) alloy belonging to a class of (FeCrAl) alloys that are considered for accident tolerant fuel cladding in light water reactors was nanostructured using two severe plastic deformation techniques of equal-channel angular pressing (ECAP) and high-pressure torsion (HPT), and their thermal stability at temperatures from 500 °C to 700 °C was studied and compared. ECAP KD was found to be thermally stable up to 500 °C, whereas HPT KD started to lose its stability at

500 °C. Microstructural characterization revealed that ECAP KD underwent recovery at 550 °C and recrystallization above 600 °C, while HPT KD showed continuous grain growth after annealing above 500 °C. Enhanced thermal stability of ECAP KD is attributed to the significant fraction (> 50%) of low-angle GBs (misorientation angle $2^{\circ} - 15^{\circ}$) stabilizing the microstructure as a result of their low mobility. Small grain sizes, a high fraction (> 80%) of high-angle GBs (misorientation angle > 15°) and accordingly a large amount of stored GB energy, serve as the driving force for HPT KD to undergo grain growth as opposed to recrystallization, which is driven by excess stored strain energy.

1. INTRODUCTION

Ultrafine-grained [UFG, average grain size (AGS) 100 nm - 1 μ m] and nanocrystalline [NC, AGS < 100 nm] metals and alloys have enhanced mechanical strength, which is attributed to the increased volume fraction of grain boundaries (GBs) providing GB strengthening [1,2]. GBs have also been shown to be effective sinks or recombination centers for irradiation-induced defects such as dislocation loops, voids, etc. [3,4]. Thus, nano-structuring is considered a good approach to improving the mechanical properties and irradiation tolerance of metals/alloys in nuclear reactors. Kanthal-D (KD, Fe-21Cr-5Al-0.026C) is one of FeCrAl alloys that are being studied to potentially replace Zr-based alloys as accident tolerant fuel cladding in light-water reactors (LWRs), owing to their superior oxidation resistance in high-temperature steam conditions [5–11].

Two severe plastic deformation (SPD) techniques, equal-channel angular pressing (ECAP) and high-pressure torsion (HPT), were employed to nano-structure commercial KD alloy bar stock in this study. Grain refinement to UFG or NC regime is possible due to the large, accumulated strains (≥ 6 – 8) during the SPD processing. SPD has been proven to enhance the strength of conventional coarse-grained (CG, AGS > 10 μm) alloys by 1.5 to 2 times due to GB strengthening and dislocation strengthening [12]. Although both ECAP and HPT are SPD techniques, the degree of grain refinement achievable is different. For example, Stolyarov et al. observed a grain size of ~150 nm after HPT of Al-2%Fe alloy in contrast with ~600 nm after ECAP [13]. Similarly, high purity Ni attained a grain size of ~170 nm after HPT as opposed to ~350 nm after ECAP [14]. This difference is due to the approach taken to grain refinement in each case. ECAP is limited to heavy straining while HPT also involves the application of high imposed pressure on the order of several GPa [15].

The degree of grain refinement is not only dependent on the corresponding SPD technique but also on the processing temperature [16–19]. Generally, the deformation temperature is preferred to be less than $0.3T_m$, where T_m is the melting temperature in K, in order to predominantly achieve 70 to 80% of high-angle GBs (HAGB, GB misorientation > 15 °) [12,20]. However, some metals and alloys cannot be processed at those temperatures owing to their limited workability. Islamgaliev et al. performed ECAP on 12Cr-2W-2Ni-0.5Mo (in wt.%) ferritic/martensitic steel at an elevated temperature of 873 K with the channels in the ECAP die intersecting at 120 degrees to avoid the formation of macroscopic defects such as cracks and fissures as a result of the steel's poor workability

[17]. An elevated temperature of 623 K enabled macroscopic defect free grain refinement in Fe-0.15C-0.25Si-1.1Mn (in wt.%) low carbon steel after ECAP as reported by Shin et al [21]. Similarly, this present study involved elevated temperature SPD to prevent the formation of discernible structural defects. ECAP was performed at 520 °C, whereas HPT was performed at 300 °C. Owing to the different temperatures and strains applied, the ECAP and HPT resulted in different microstructures with differences in dislocation density, grain boundary character and grain size [22].

However, the thermal stability of SPD produced UFG, or NC alloys is a concern. Due to the presence of a significant volume fraction of GBs after SPD, there is an increase in the stored GB energy, which serves as the driving force for grain growth during thermal annealing. In addition, an increase in the stored strain energy after SPD (due to increased dislocation density) drives recrystallization, which is a two-step process consisting of nucleation of strain-free grains followed by their growth. Recrystallization in UFG or NC alloys leads to an increase in grain size, a result similar to that from grain growth, although recrystallization and grain growth are two different physical processes. The occurrence of grain growth or recrystallization during thermal annealing defeats the purpose of grain refinement using SPD. Therefore, it is important to study and understand the thermal stability of these ECAP or HPT produced materials to assess them for potential applications in high-temperature environments like nuclear reactors.

This study is the first to compare the microstructures between ECAP and HPT processed FeCrAl alloy and investigate the impact of the microstructural differences on

the thermal stability, as well as understand the mechanisms responsible for the microstructure evolution during thermal annealing.

2. EXPERIMENTAL

Cylindrical KD commercial bar stock (composition provided in Table 1) was subjected to solution treatment at 1050 °C (above the austenitization temperature A3) for 1 h, followed by oil quenching and tempering at 800 °C for 1 h to obtain fully ferritic microstructure, before air cooling down to room temperature (hereafter referred to as 'heat treated KD bar stock').

Table 1. Elemental composition of KD.

Element	Fe	Cr	Al	Ni	Si	Mn	Zr	V	С	Ti,Co
Wt.%	Bal.	20.570	4.790	0.260	0.240	0.180	0.150	0.030	0.026	0.020

ECAP was carried out on heat-treated KD bar stock at a temperature of 520 °C up to six passes following the B_c route [23]. The inner contact angle between the channels of the ECAP die was 120°. Some of the heat-treated KD bar stock was sectioned to ~2 mm thick discs, and HPT was performed on the discs with a diameter of ~20mm under a pressure of 6 GPa at 300 °C for ten rotations, at 0.2 rotations per minute [24]. The final thickness of the discs after HPT was measured to be ~1.2 mm. Annealing was performed in an alumina tube furnace under an Ar atmosphere with a heating rate of 10 °C/ min to

attain the desired temperature. Annealing of ECAP KD was performed in Ar atmosphere at the temperatures of 500 °C, 550 °C, 600 °C, 650 °C and 700 °C for 3h, 6h, 12h, 24h and 48h at each temperature. Annealing of HPT KD was performed in Ar atmosphere at the temperatures of 500 °C, 550 °C, and 600 °C for 3h, 6h, 12h, 24h, and 48h at each temperature. The reason why annealing of HPT was not carried out at 650 °C and 700 °C will be addressed later in the paper.

A Phillips X'PERT MPD with a Cu source was used to perform X-ray diffraction (XRD). Rietveld refinement of the obtained XRD data was performed using MAUD software to determine the dislocation density. Electron backscatter diffraction (EBSD) and transmission kikuchi diffraction (TKD) were performed using an Oxford HKL EBSD system, in an FEI Helios NanoLab 600 scanning electron microscope (SEM) to quantify GB character and grain size. Samples for EBSD were prepared meticulously by mechanical polishing, using colloidal silica with particle size down to 0.02 µm for 45 min. The indexing/hitting rate for annealed/ECAP KD was 90-95% and annealed/HPT KD was 85-90%. Post processing of EBSD data was performed using Channel5 and cleaning of the EBSD misorientation maps was carried out following ASTM E2627-10 [25].

APT specimens were fabricated using standard lift-out and sharpening methods as described by Thompson *et al.* using a Thermo Fisher Nova 200 Dual Beam scanning electron microscope/focused ion beam (SEM/FIB) [26]. The APT experiments were run using a CAMECA LEAP 4000XHR in laser mode with a 30K base temperature, 60 pJ laser power, and a 0.5% detection rate. The APT results were reconstructed and analyzed using CAMECA's interactive visualization and analysis software (IVAS 3.8). TKD lamellas and

LEAP tips were prepared via a standard focused ion beam (FIB) lift-out procedure. Vickers microhardness was obtained using a Struers Duramin5 Vickers hardness tester applying a force of 4.91 N for 5 sec. Miniature (mini) tensile testing was carried out using a tabletop lnstron 5969 universal testing system with 50 kN load cell at a quasi-static strain rate of 10^{-4} /sec. The sample dimensions for mini-tensile testing are provided below in Figure 1. The mini-tensile dog bone specimens were prepared using wire electric discharge machining (EDM).

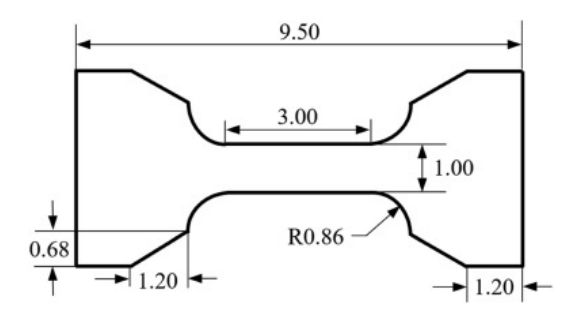


Figure 1. Engineering drawing of the specimen used for mini-tensile testing in this study (all dimensions in mm). The thickness of the specimen is 1mm.

3. RESULTS

3.1. THERMAL STABILITY OF ECAP KD

ECAP KD has an inhomogenous microstructure with a multi-modal grain size distribution as reported by the authors previously [27]. Predominantly, two grain size ranges were found in ECAP KD. They were fine-grained (FG, AGS 1-10 μ m) and UFG (AGS 100 nm - 1 μ m). The fine grains have low-angle GBs (LAGBs, GB misorientation 2 – 15°) in the grain interior implying early stages of grain refinement [22]. The overall area fraction of HAGBs in ECAP was found to be ~51% from EBSD.

Figure 2a displays plots of Vickers microhardness vs. annealing time at temperatures between 500 and 700 °C, indicating the thermal stability/instability of ECAP KD. The as-deformed average hardness of ECAP KD was measured to be 333 ± 17 HV. The relatively large standard deviation came from the broad grain size distribution. The hardness of ECAP KD after annealing at 500 °C for 3h, 6h, 12h, and 24h was within ±10 HV (within error) from the hardness of ECAP KD. The same behavior was observed at 550 °C until an annealing time of 24h; however, when annealed for 48h, the average hardness dropped to 292 ± 19 HV (12%). EBSD orientation map of ECAP KD annealed at 550 °C for 48h shown in Figure 2b revealed a microstructure with a measured area fraction of LAGBs of ~50%, which is essentially identical to that in as-processed ECAP KD. The decrease in hardness without considerable change in the microstructure is ascribed to static recovery leading to a reduction in dislocation strengthening [28]. The probability for dislocationdislocation interaction is higher in FG microstructure compared to that in UFG microstructure as dislocation-GB interaction comes into play [29-31]. With ECAP KD having both FG and UFG microstructures, it is possible that the extent of loss of dislocation strengthening is higher in the regions consisting of fine grains in comparison to that in the regions comprising of ultrafine grains. Thus, when measuring the bulk hardness of ECAP KD post static recovery (after annealing at 550 °C for 48 h), it is expected that the range of hardness measured is wider. This could be the reason behind the increase in the hardness error to 19 HV post annealing at 550 °C for 48 h.

A drop in hardness of ~20 HV (6%) and ~40 HV (12%) is observed in ECAP KD annealed at 600 °C for 3h and 6h, respectively. However, a significant drop of ~80 HV

(24%) is observed after annealing at 600 °C for 12h. EBSD orientation maps were obtained from ECAP KD annealed at 600 °C for 6h and 12h as shown in Figures 2c and 2d, respectively, to understand the reason for the drop in hardness. The sample annealed at 600 °C for 12h exhibits an equiaxed microstructure with a higher area fraction of HAGBs. The percentage of HAGBs increased from ~51% in as-processed ECAP KD to ~80% in ECAP KD annealed at 600 °C for 12h. The corresponding reduction in the percentage of LAGBs from ~49% to ~20% and evolution to an equiaxed microstructure after annealing suggest that the material has undergone recrystallization. As addressed earlier, the strain imposed in the matrix serves as the driving force for recrystallization. Strain is manifested in the matrix in the form of dislocations distorting the matrix. From XRD, the dislocation density in the as-processed ECAP KD was estimated to be $1.2 \times 10^{14} \,\mathrm{m}^{-2}$. The inhomogeneous microstructure of the ECAP KD annealed at 600 °C for 6h with a large area-fraction of LAGBs (>50%), as disclosed by the EBSD orientation map in Figure 2c, is similar to that of the as-processed ECAP KD.

Nevertheless, onset of recrystallization, indicated by recrystallized grains (as pointed out by black arrows in Figure 2c) that nucleated out of pre-existing HAGBs, occurred at this stage of annealing. Figure 2e and 2f show the GB misorientation angle distribution in ECAP KD annealed at 600 °C for 6h and 12h, respectively. A higher fraction of HAGBs is evident in the latter than in the former. This can also be considered as evidence for recrystallization, suggesting that the strain stored in the LAGBs (array of dislocations) is relieved by nucleation of strain-free grains [32].

Figure 2a shows a drop in hardness of ~80 HV (24%) and ~90 HV (27%) after annealing ECAP KD at 650 °C for 6h and at 700 °C for 3h, respectively. EBSD orientation maps obtained after annealing at 650 °C for 6h and at 700 °C for 3h are presented in Figures 3a and 3b, respectively. Equiaxed microstructures with area fractions of HAGBs of 81% and 83.6% (Figure 3c and 3d), respectively, are evident, which are very similar to the recrystallized microstructure observed after annealing at 600 °C for 12h (Figure 2d). Thus, as the temperature increased from 600 °C to 700 °C, the time required for recrystallization to occur was decreased from 12h to 3h. If the annealing temperature is further increased (>700 °C), it is possible that recrystallization could occur in less than 3h.

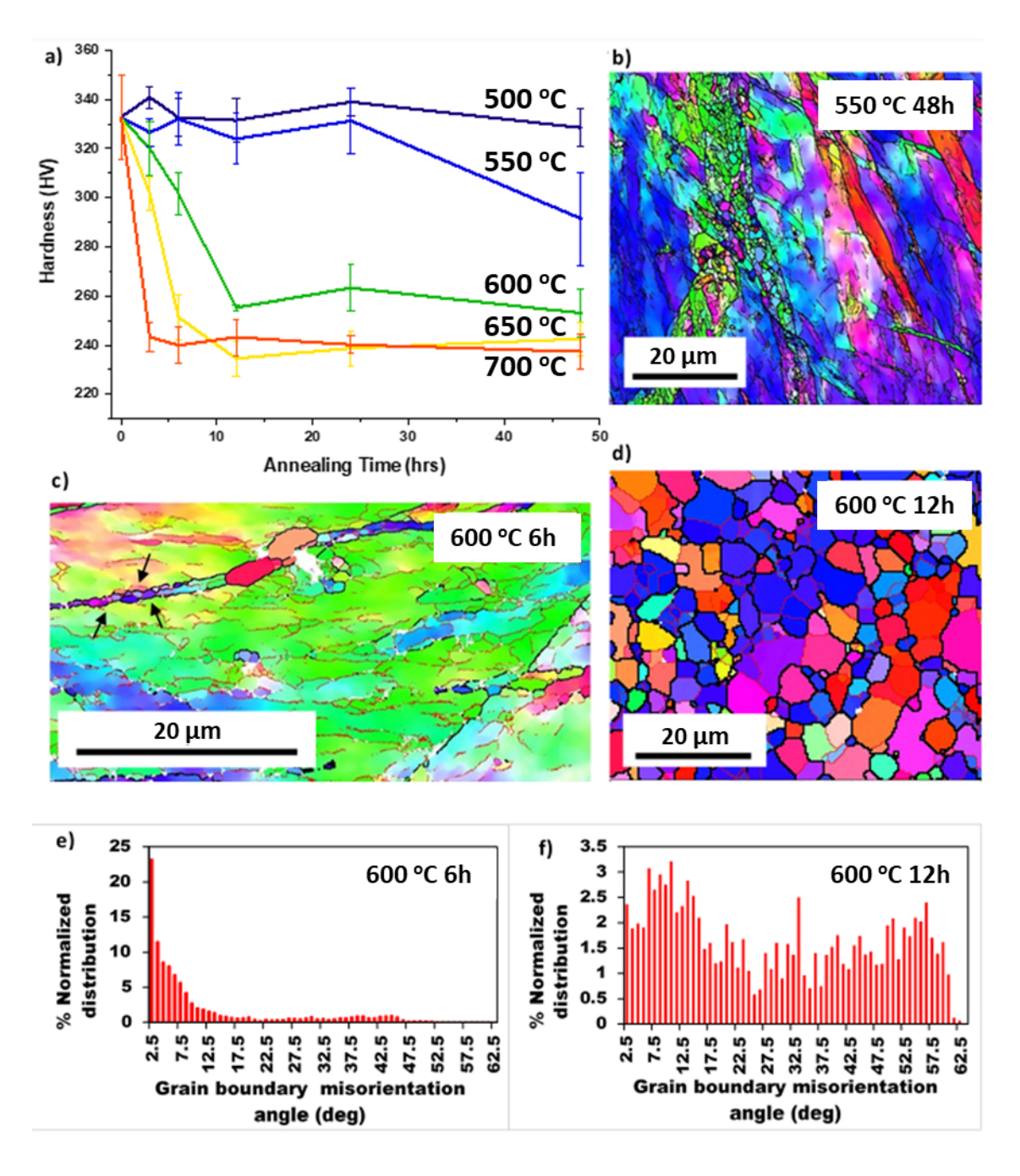


Figure 2. a) Vickers microhardness versus annealing time for temperatures of 500 °C, 550 °C, 600 °C, 650 °C, and 700 °C. b) EBSD orientation map obtained from ECAP KD after annealing at 550 °C for 48h. c) EBSD orientation map after annealing at 600 °C for 6h. d) EBSD orientation map after annealing at 600 °C for 12h. e) GB misorientation angle distribution in ECAP KD annealed at 600 °C for 6h. f) GB misorientation angle distribution in ECAP KD annealed at 600 °C for 12h.

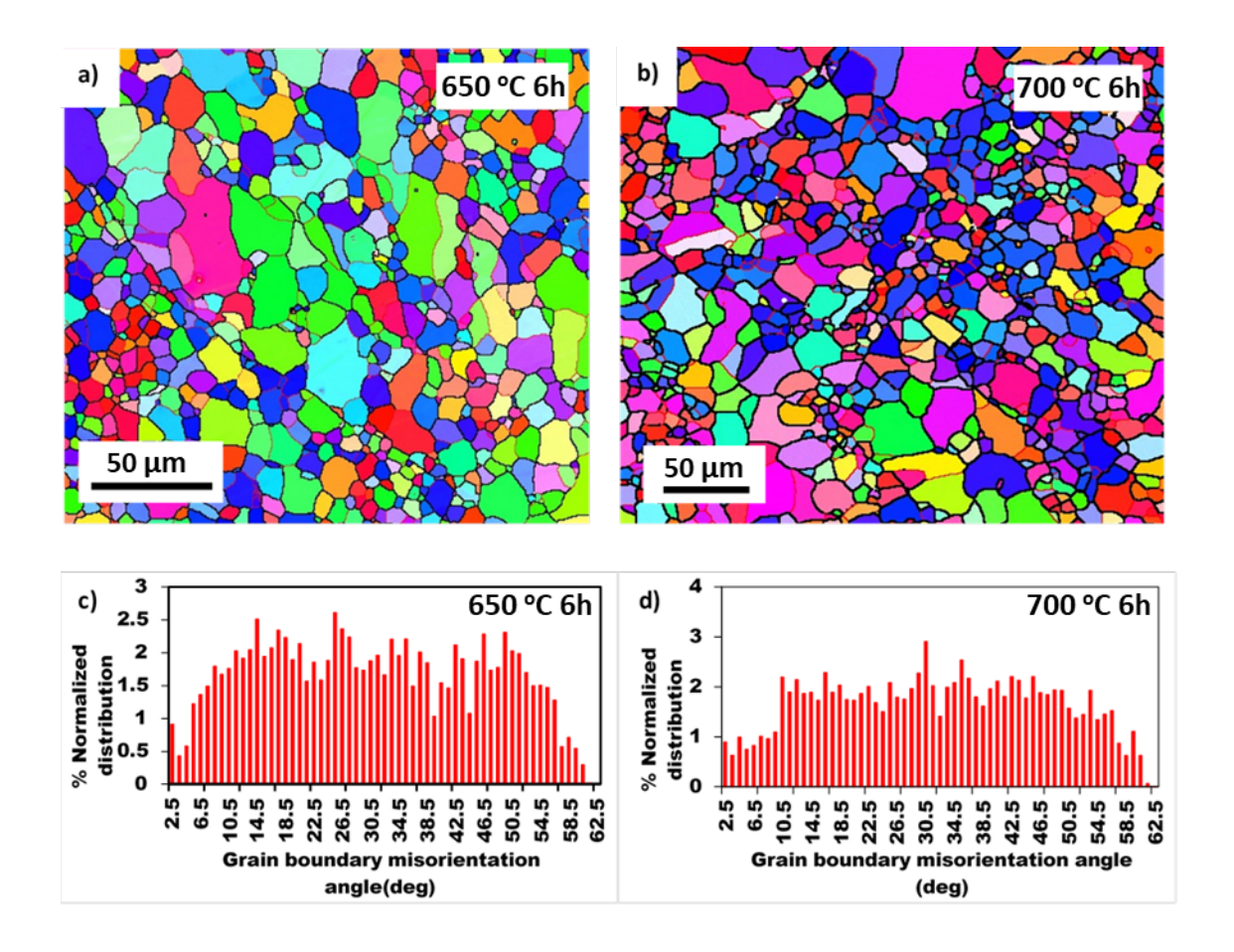


Figure 3. a) EBSD orientation map of ECAP KD after annealing at 650 °C for 6h. b) EBSD orientation map of ECAP KD after annealing at 700 °C for 6h. c) GB misorientation angle distribution in ECAP KD annealed at 650 °C for 6h. d) GB misorientation angle distribution in ECAP KD annealed at 700 °C for 6h.

Figure 4 shows the XRD patterns of as processed and annealed ECAP KD. ECAP KD annealed at 550 °C for 6h, 12h, 24h and 48h all have a texture very similar to that in asprocessed ECAP KD. An increase in the peak intensity to peak width ratio for (200) and (211) is observed with increasing annealing time. Comparing this observed trend with the thermal stability of ECAP KD at 550 °C in Figure 2a, as well as the EBSD orientation map after annealing at 550 °C for 48h in Figure 2b, it can be concluded that static recovery occurs at 550 °C in ECAP KD. Static recovery results in a decrease in dislocation density

owing to annihilation of dislocations in the matrix. This is expected to reduce the strain in the matrix, thereby reducing peak broadening and increasing peak intensity to peak width ratio in the XRD patterns [33]. In contrast to Figure 4a, Figure 4b shows a noticeable change in texture for ECAP KD annealed at 600 °C for 6h, and at 650 °C for 6h; an increase in the intensity of peaks corresponding to (200) and (211) crystallographic planes are evident for these samples. From EBSD, ECAP KD annealed at 600 °C for 6h is at the onset of recrystallization, and ECAP KD annealed at 650 °C for 6h has a recrystallized microstructure as established in Figures 3a and 3c. These observations indicate that there is a change in texture during recrystallization in ECAP KD.

In summary, ECAP KD is thermally stable up to 500 °C as revealed by the Vickers microhardness vs annealing time plot (Figure 2a). EBSD analysis reveals a recrystallized microstructure after annealing ECAP KD at 600 °C for 12h (Figure 2d). Time to recrystallize decreases with increases in annealing temperature. Recrystallization, i.e., nucleation of strain-free grains and their subsequent growth, introduces a change in texture as disclosed by XRD.

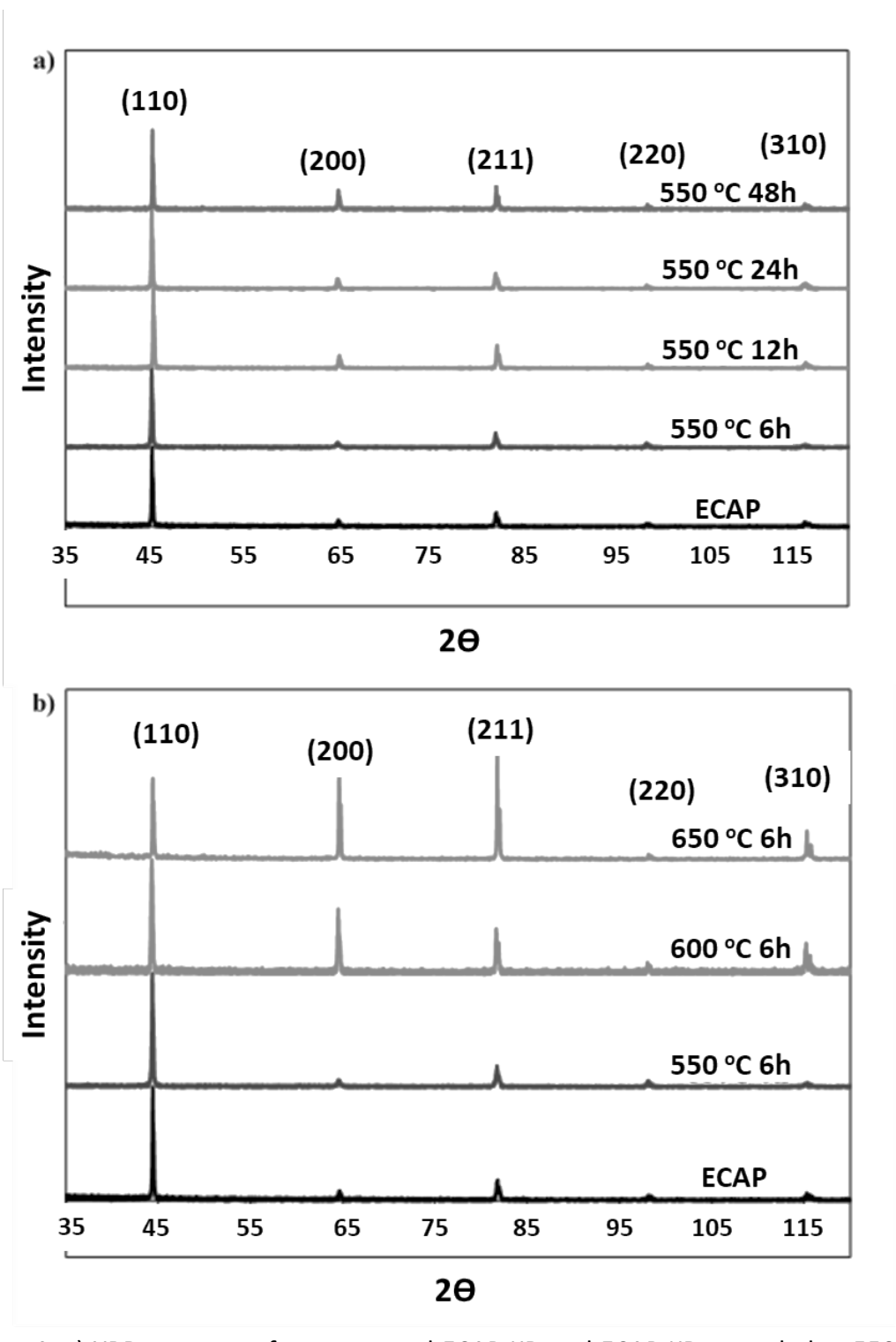


Figure 4. a) XRD patterns of as-processed ECAP KD and ECAP KD annealed at 550 $^{\circ}$ C for 6h, 12h, 24h and 48h. b) XRD pattern of as-processed ECAP KD and ECAP KD annealed at 550 $^{\circ}$ C for 6h, 600 $^{\circ}$ C for 6h and 650 $^{\circ}$ C for 6h.

3.2. THERMAL STABILITY OF HPT KD

We have previously reported that HPT KD has a nanocrystalline grain size (AGS = 75 ± 39 nm) [27]. TKD was performed to obtain the GB characteristics in HPT KD since conventional EBSD does not have the required resolution to resolve nanocrystalline grains. GB misorientation angle distribution in Figure 5b indicates that as-processed HPT KD has an area fraction of HAGBs of ~84.5%, which is ~33.5% higher than that in ECAP KD. This suggests that HPT KD has a higher GB energy compared to ECAP KD [34].

Torsional strain applied to a specimen during HPT is directly proportional to its radius [35]. The degree of grain refinement is the least at the center due to the lowest imposed torsional strain there. This is reflected in the mechanical properties in accordance with the Hall-Petch relationship [36], where the microhardness is ~90 HV lower than the areas beyond a distance of 2 mm from the center as can be seen in Table 2. For this reason, in this study, the microstructures of as processed and annealed HPT KD were obtained beyond 2 mm from the center where the hardness is relatively uniform (within error) regardless of the distance from the center.

Table 2. Hardness profile of HPT Kanthal-D from center to circumference.

Distance from center (mm)	0 (Center)	2	4	6	8
Average Vickers microhardness (HV)	513 ± 6	599 ± 10	605 ± 3	605 ± 10	598 ± 12

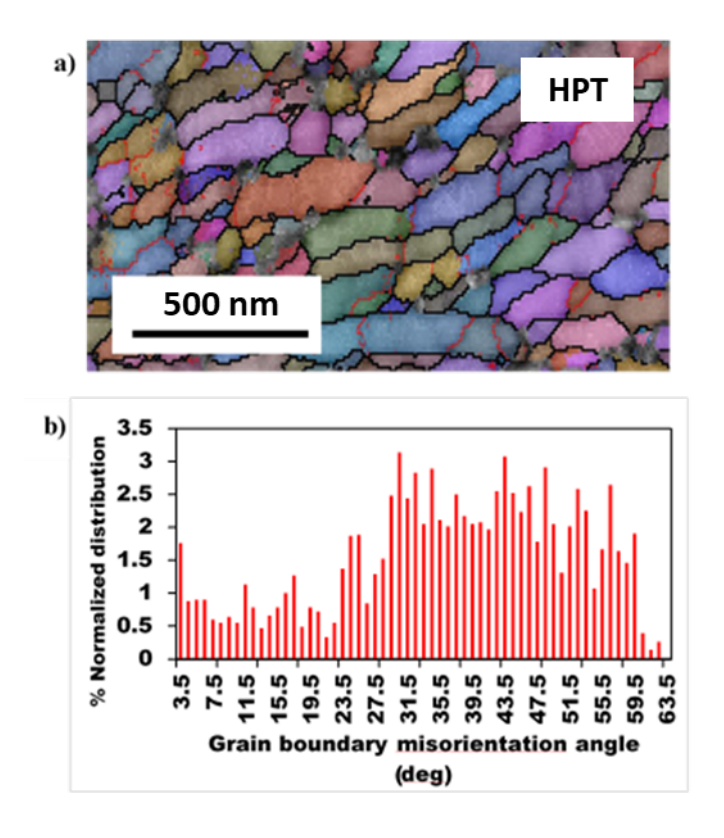


Figure 5. a) Transmission Kikiuchi Diffraction orientation map of HPT KD from the longitudinal direction. b) GB misorientation angle distribution in HPT KD.

The same annealing scheme used for ECAP KD was used to assess the thermal stability of HPT KD; however, temperature varied only between 500 °C and 600 °C as shown in Figure 6a. A drastic drop in hardness of ~180 HV (30%) was observed after 3h of annealing at 500 °C from the initial average hardness of 595 ± 11 HV of as-processed HPT KD. The reason why there is no error bar for HPT KD annealed at 500 °C for 48h is that the measured hardness was exactly the same regardless of the location of measurement. Although hardness trends upwards post annealing at 500 °C for 24h and 500 °C for 48h, it is within hardness error of HPT KD annealed at 500 °C for 12 h. Higher drops in hardness of ~250HV (42%) and ~310HV (52%) were recorded after 3h of annealing at 550 °C and

600 °C, respectively. Since HPT KD was found thermally unstable at 600 °C and lower, annealing at higher temperatures was not carried out. This behavior is different from that of ECAP KD, which is stable up to 500 °C.

EBSD orientation maps obtained from HPT KD annealed at 550 °C for 3h, 6h and 24h, as displayed in Figures 6 b, c, and d, respectively, show equiaxed microstructures with AGS greater than that of as-processed HPT KD. The microstructure in each case is indicative of continuous grain growth as opposed to that of annealed ECAP KD (which exhibited classic static recrystallization). The AGS of HPT KD annealed at 550 °C for 3h, 6h, and 24h, was found to be 690 ± 440 nm, 800 ± 490 nm, and 1280 ± 870 nm, respectively.

The dislocation density obtained from XRD in HPT KD is 1.0×10^{15} m⁻², which is approximately an order of magnitude higher than 1.2×10^{14} m⁻² in ECAP KD. This suggests that in addition to a higher GB energy than ECAP KD, HPT KD also has a higher stored strain energy, providing a driving force for recrystallization [24]. Thus, it appears possible that recrystallization occurred early in the annealing yielding an inhomogeneous microstructure (similar to that of annealed ECAP KD, which is represented by ECAP KD annealed at 700 °C for 3h in Figure 3b) and broad grain size distribution. On prolonged annealing (\geq 3h), the second step of recrystallization (growth of recrystallized grains) could have led to the formation of a more homogeneous microstructure representative of continuous grain growth.

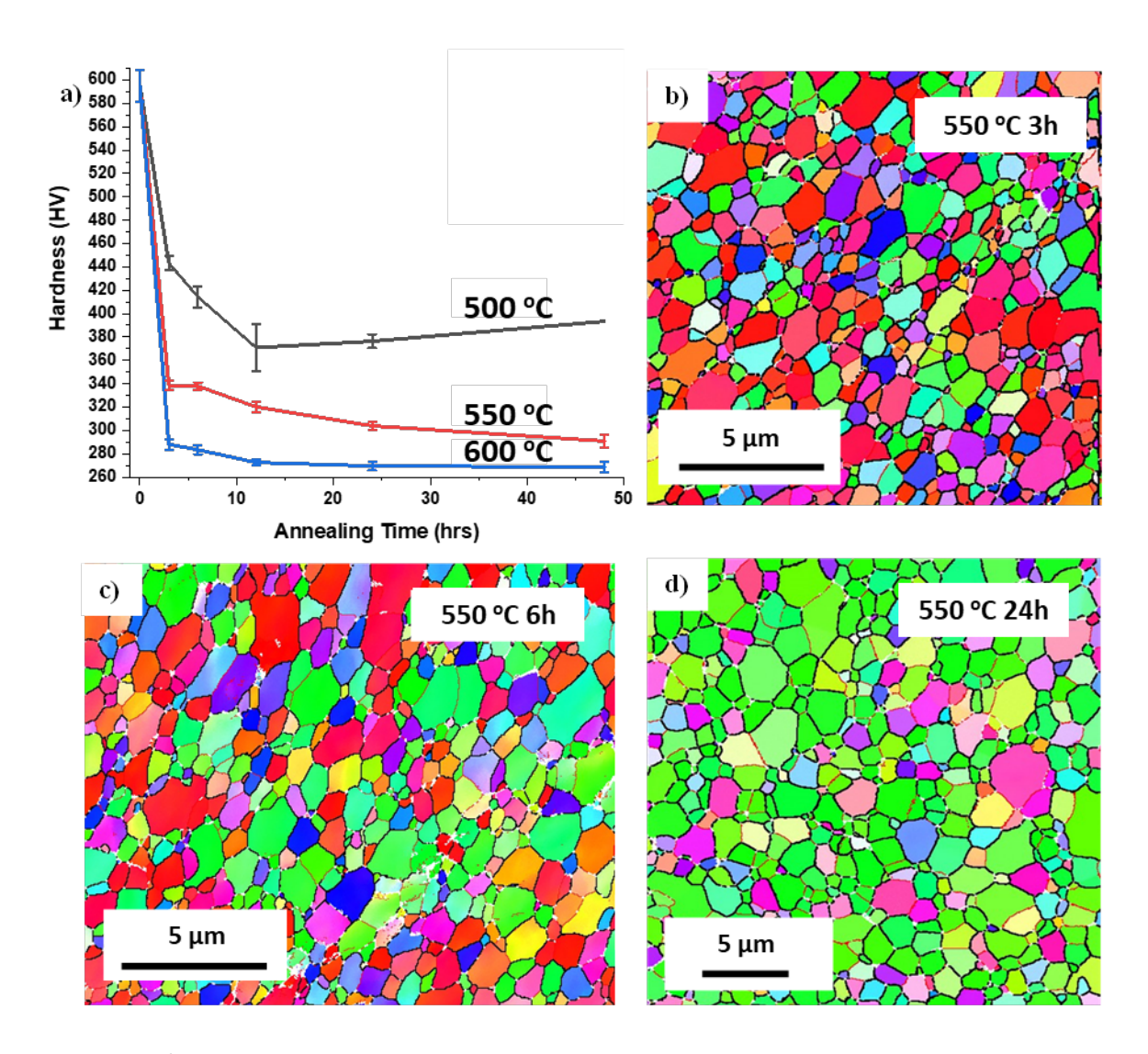


Figure 6. a) Vickers microhardness vs annealing time for HPT KD at temperatures of 500 °C, 550 °C and 600 °C. b) EBSD orientation map of HPT KD annealed at 550 °C for 3h. c) EBSD orientation map of HPT KD annealed at 550 °C for 6h. d) EBSD orientation map of HPT KD annealed at 550 °C for 24h.

In order to verify whether or not recrystallization had taken place within a span of few minutes, HPT KD was annealed at 500 °C for 10 min, 20 min and 30 min, and EBSD maps were obtained to analyze the microstructure. The Vickers microhardness vs. annealing time plot in Figure 7a indicates that the hardness of HPT KD dropped to 531 ±

11 HV (~10% drop) after annealing at 500 °C for 10 min. The corresponding EBSD orientation map in Figure 7b shows a microstructure with an average grain size of 200 ± 90 nm. After annealing at 500 °C for 20 min and 30 min, the hardness was 529 ± 4 HV (~10% drop) and 532 ± 9 HV (~10% drop), respectively; the variation in hardness as a function of annealing time is within the error bars. After annealing at 500 °C for 20 min and 30 min, the AGS was 200 ± 100 nm and 210 ± 110 nm, respectively, very similar to that of HPT KD annealed at 500 °C for 10 min. The HAGB fraction in the HPT KD annealed at 500 °C for 10, 20, and 30 min is between ~82-84%, which is comparable to that in the as-deformed HPT; in the EBSD orientation maps, HAGBs are in black and LAGBs are in red. Thus microstructural evolution after annealing HPT KD at 500 °C for 10 min, 20 min and 30 min is indicative of classic continuous grain growth, similar to that observed in HPT KD after longer durations of annealing.

If only continuous grain growth occurred in HPT KD after annealing, it is anticipated that a decrease in XRD peak width and increase in peak intensity will be observed for all the peaks corresponding to the different characteristic crystallographic planes due to a reduction in strain and increase in grain size [37]. XRD was performed on as-processed HPT KD and those annealed. The comparison of XRD patterns in Figure 8 indicates no significant change in texture associated with the hardness drop after annealing HPT KD at 500 °C for 3h. However, it can be observed that HPT KD has broad (110), (211), and (220) peaks compared to those of the annealed samples; this is especially evident in the case of the highlighted (110) peak. This is due to the fact that the asprocessed HPT KD has a smaller grain size and higher strain compared to the annealed

samples. The reduction in peak width with no appreciable change in texture, combined with the microstructural examination, suggests that HPT KD only underwent continuous grain growth during annealing, without the occurrence of recrystallization.

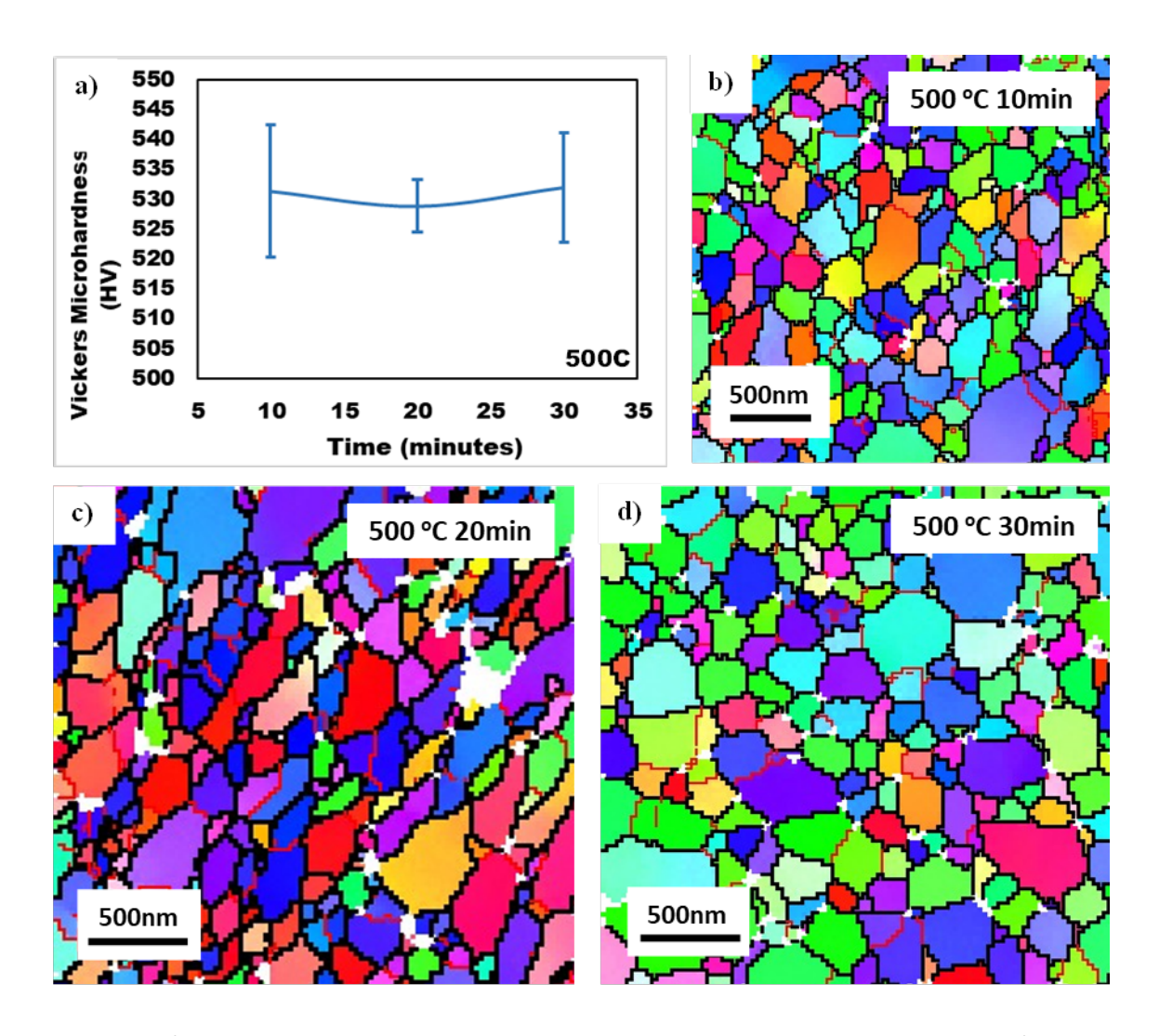


Figure 7. a) Vickers microhardness of HPT KD vs annealing time at 500 $^{\circ}$ C. b) EBSD orientation map of HPT KD annealed at 500 $^{\circ}$ C for 10 min. c) EBSD orientation map of HPT KD annealed at 500 $^{\circ}$ C for 20 min. d) EBSD orientation map of HPT KD annealed at 500 $^{\circ}$ C for 30 min.

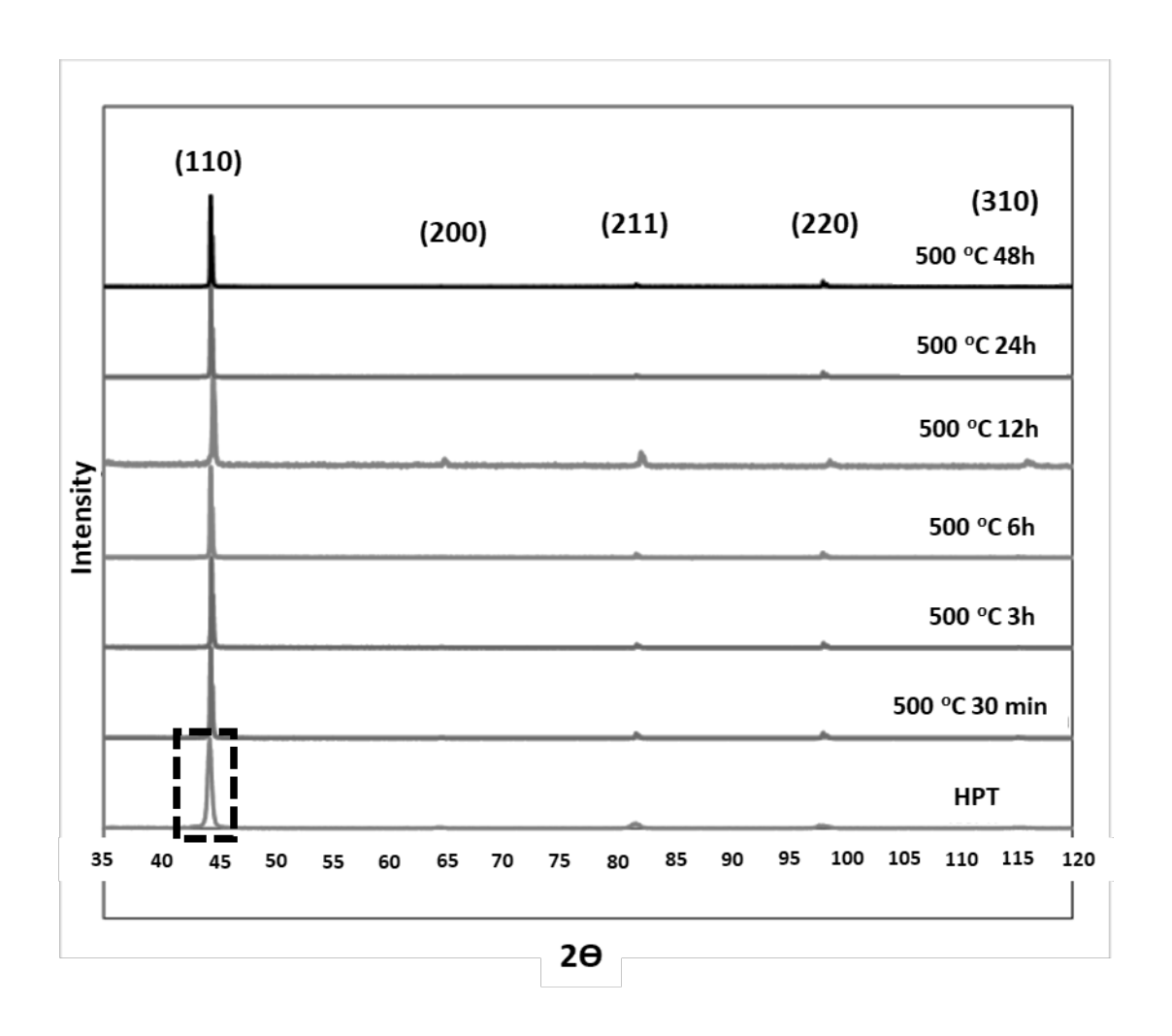


Figure 8. XRD patterns of as-processed HPT KD and HPT KD annealed at 500 $^{\circ}$ C for 30 min, 3h, 6h, 12h, 24h, and 48h.

3.3. MINI-TENSILE TESTING OF ANNEALED AND AS-PROCESSED KD

Owing to the non-homogeneity of as-deformed ECAP microstructure (FG and UFG), it is important to confirm the validity of microhardness testing results using a different mechanical testing technique. Thus, miniature tensile testing was perfomed. Figure 9 shows the engineering stress-strain curves of CG KD, as-processed ECAP KD, and annealed ECAP KD. The ultimate tensile strength (UTS) of CG KD and ECAP KD was measured to be 490 MPa and 802 MPa, respectively. The UTS of ECAP KD is ~1.63 times

that of CG KD, which is an outcome of dislocation strengthening and GB strengthening [12]. Vickers microhardness of CG KD and ECAP KD was measured to be 228 ± 4 HV and 333 ± 17 HV, respectively. The microhardness of ECAP KD is ~1.46 times that of CG KD. After ECAP processing, the increase in UTS is more than that in microhardness.

Results on the thermal stability of ECAP KD presented in Section 3.1 indicate that the sample is stable up to 500 °C. Consistent with that observation, ECAP annealed at 500 °C for 12h exhibits a UTS of 783 MPa, which is only 19 MPa less than that of as-processed ECAP KD. This minimal decrease in strength by 2.3% is within the error for UTS of as-processed ECAP KD. The microhardness of ECAP annealed at 500 °C for 12h (331 \pm 9 HV) is also very similar to that of as-processed ECAP KD. Both tensile and hardness testing reinforce the fact that ECAP KD is stable at 500 °C.

The drop in strength after recrystallization is reflected in the UTS of ECAP KD annealed at 700 °C for 12h, which is only ~40 MPa higher than that of CG KD. A similar trend was also observed in the case of the microhardness testing with ECAP KD annealed at 700 °C for 12h showing hardness of 243 ± 7 HV, which is only 20 HV higher than that of CG KD. The notable decrease in strength after recrystallization is due to removal of dislocation strengthening and GB strengthening. Overall, the results of the miniature tensile testing are in agreement with those of the microhardness testing and microstructural characterization. Miniature tensile testing was not extended to HPT KD owing to the small sample dimensions.

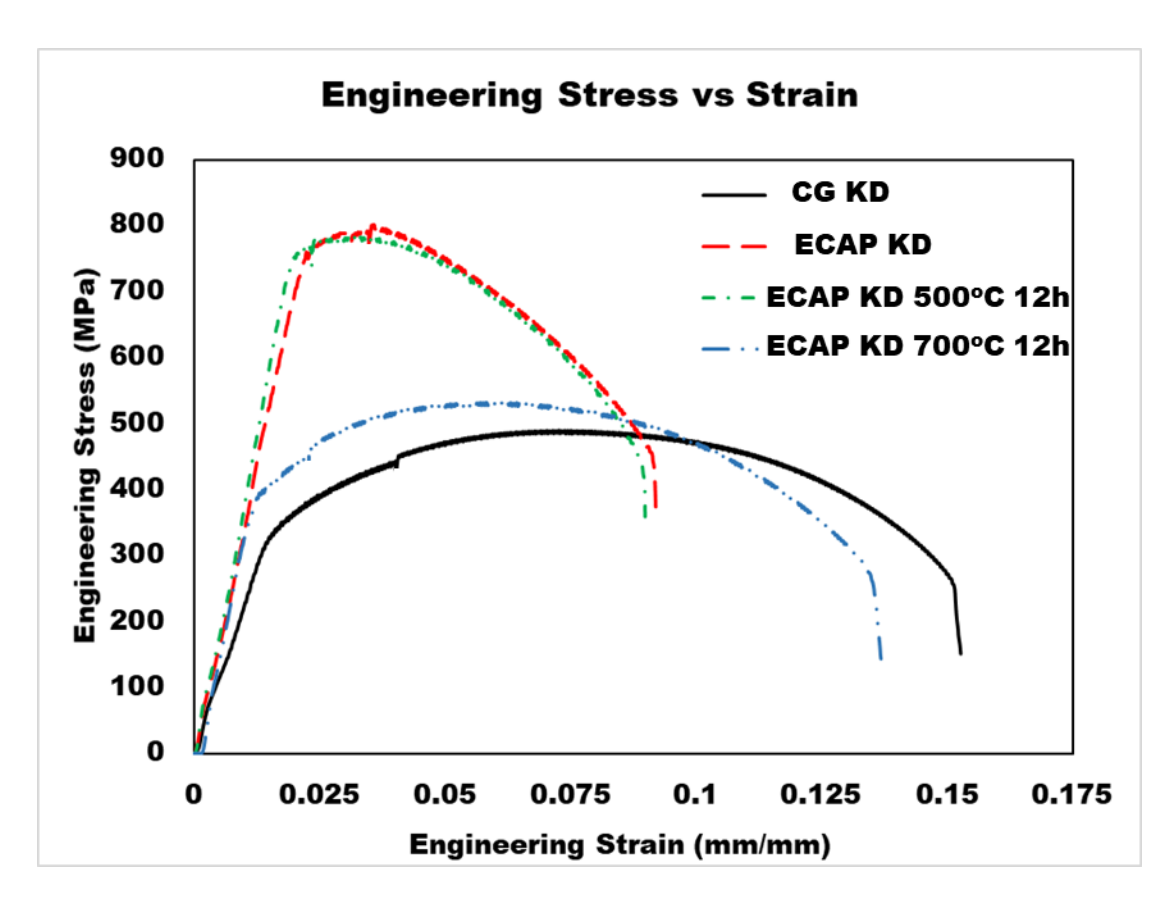


Figure 9. Engineering stress-strain curves of CG KD, as-processed ECAP KD and annelaed ECAP KD.

4. DISCUSSION

4.1. INFLUENCE OF GB MOBILITY ON THERMAL STABILITY

The performance of a polycrystalline metal/alloy in a thermo-mechanical environment is closely related to the three dimensional network of GBs [34]. A higher volume fraction of GBs increases the strength of metals/alloys by impeding dislocation motion that enables plastic deformation [38]. For nuclear applications, GBs have also been shown to be effective sinks for irradiation-induced defects such as point defects,

dislocations, dislocation loops, and voids; such defects migrate towards GBs and get annihilated at the GBs [39].

However, there is excess interfacial energy associated with GBs. When these materials are heated to a temperature that is an appreciable fraction of the melting point, the GBs migrate and grains grow to decrease the GB area and reduce the excess GB energy, pushing the alloy closer to equilibrium [40]. Several approaches have been developed to stabilize these GBs in the non-equilibrium state. Thermodynamically, segregation of solutes, as well as precipitation of secondary-phase particles along GBs in certain cases, has been shown to decrease the interfacial energy thereby stabilizing GBs in UFG and NC metals/alloys [41–45]. Kinetically, solutes segregated to GBs drag GBs (i.e. solute drag) and second-phase particles pin GBs from migrating. The abovementioned approaches require modification of the alloy composition, which may not be desirable for all applications. Apart from that, segregation of the solute atoms and precipitation of a secondary phase may also lead to phase instabilities [46,47].

The velocity of a moving GB is equal to the driving force times the mobility of the GB. Thus, a reduction in the mobility of GBs retards their migration. Inherently, GB mobility is affected by the misorientation angle of the GB [40]. In this study, the GB misorientation angle distributions in as-processed ECAP KD and HPT KD are different. As-processed ECAP KD exhibits a higher fraction (>40%) of LAGBs than HPT KD, whereas HPT KD consists of a higher fraction of HAGBs. This disparity in the GB character leads to variation in GB mobility, which in turn affects the thermal stability. LAGBs are built of an array of dislocations as opposed to HAGBs that in general possess a disordered structure

[15,48]. Dislocation cell walls or LAGBs are formed prior to the formation of HAGBs during SPD. Transformation from a cellular structure to a granular structure occurs in two steps. The first step is the partial annihilation of dislocations with different signs leading to the formation of a high density of dislocations with a burgers vector perpendicular to the boundary. The second step involves the compounding of such dislocations reaching a threshold beyond which grain formation (misorientation>15°) occurs [49]. This suggests that the mobility of LAGBs is controlled by dislocation motion in contrast to the motion of random HAGBs that is governed by GB diffusion.

In order to be cohesive structurally, the mobility of LAGBs depends on the rate at which dislocations undergo climb [48,50–52]. The rate of dislocation climb depends on the lattice diffusion, which has been shown to have a lower enthalpy of activation in contrast with that for GB diffusion [53–56]. For perspective, Winning et al. reported an increase of two orders of magnitude in mobility of GBs when the misorientation angle increased from below 10° to above 15° in pure Al. Along with lower inherent mobility, the motion of LAGBs is further reduced by pinning of other network dislocations. In contrast, higher mobility of HAGBs was ascribed to the absorption of network dislocations during their migration along with their innate tendency to move faster [57]. Analogous behavior is expected for the nanostructured FeCrAl system on annealing. The higher fraction of LAGBs in ECAP KD is expected to stabilize the grain structure up to 500 °C, whereas HPT KD is unstable at that temperature as a result of high fraction of highly mobile HAGBs.

The current FeCrAl system is very similar to that of Winning et al. in the sense that, along with dislocations that make up the LAGBs, dislocation networks exist in both ECAP

and HPT KD. Therefore, it is expected that these dislocation networks hinder the motion of LAGBs owing to complex dislocation interactions, thereby enhancing thermal stability of ECAP KD [58]. In contrast, in HPT KD, these dislocation networks are consumed by HAGBs in the course of GB migration. In conclusion, the improved thermal stability of ECAP over HPT KD is accredited to an increased fraction of LAGBs with low mobility stabilizing the microstructure. The difference in the thermal stability of ECAP and HPT KD is attributed to the differences in the distribution of GB misorientation angles.

4.2. GRAIN GROWTH IN HPT KD VERSUS RECRYSTALLIZATION IN ECAP KD

From XRD, it was estimated that the dislocation density in ECAP KD is an order of magnitude lower than that in HPT KD. This suggests that HPT KD has a higher stored excess strain energy than ECAP KD. This would prompt the idea that HPT KD should have undergone recrystallization during annealing [59]. However, HPT KD has an AGS of 75 ± 39 nm, whereas FG (AGS 1- 10 μm) and UFG (AGS 100 nm - 1 μm) grain size ranges are present in ECAP KD; therefore, the AGS of HPT KD may be >10 times smaller than that of the FG region in ECAP KD, and the density or volume fraction of GBs is much higher in HPT KD than in ECAP KD. In addition, out of the GBs in HPT KD, ~85% of them are HAGBs, which have higher energy than LAGBs. Thus, HPT KD has more than an order of magnitude higher GB energy than ECAP KD. This excess stored energy at the GBs is further increased in SPD metals/alloys owing to the presence of a very high defect density making them non-equilibrium GBs. It is energetically favorable for these highly deformed GBs to relieve this excess energy by undergoing GB migration (i.e., grain growth) instead of

recrystallization [15,60,61]. These non-equilibrium HAGBs in HPT KD are homogeneously distributed throughout the material. Therefore, it is expected that they migrate homogeneously resulting in a microstructure representative of continuous grain growth as corroborated by the EBSD orientation maps of the annealed HPT KD.

In ECAP KD, there is not a homogeneous distribution of LAGBs and HAGBs. Regions of UFGs and fine grains are both present. It is anticipated that the high fraction of LAGBs (>50%) in ECAP KD interact with the dislocation networks in the grain interiors in such a way that there is only limited recovery [62–65]. That is, the strain in the grain interiors is not removed by the movement of LAGBs. This non-equilibrium microstructure possesses and preserves a high driving force (i.e., stored excess strain energy) for recrystallization, and the activation energy for recrystallization is reduced. ECAP KD gains the required activation energy for recrystallization to occur at 600 °C, relieving the strain and transforming to a microstructure with ~80% HAGBs as indicated by EBSD results. With an increase in the annealing temperature to 650 °C and 700 °C, the rate at which recrystallization occurs is accelerated. Hence, recrystallized microstructures are evident after 6h and 3h at 650 °C and 700 °C, respectively, in contrast with 12h at 600 °C. The nucleation and subsequent growth of new grains in ECAP KD lead to a change in the texture of the material, as indicated by the XRD results in Figure 4. In contrast, the XRD patterns of annealed HPT KD (Figure 8) only showed the narrowing and sharpening of the peaks, without any change in texture. That is, due to the removal of strain and increase in the average grain size from grain growth, XRD peaks become narrower [31]. This further bolsters the argument that HPT KD underwent continuous grain growth instead of recrystallization during annealing.

4.3. INFLUENCE OF SOLUTE SEGREGATION AND SECOND-PHASE PARTICLES ON THERMAL STABILITY

Solute segregation can occur along GBs, which reduces their free energy and mobility, thereby increasing the thermal stability. LAGBs have been reported to exhibit a smaller amount of solute segregation in comparison to HAGBs, owing to their smaller misorientation angle and lower energy [66–68]. Accordingly, a higher degree of solute segregation may have occurred in HPT KD than in ECAP KD, owing to the higher fraction of HAGBs in HPT KD. In addition, the higher defect concentration in HPT KD as compared to ECAP KD leads to enhanced diffusion, thereby resulting in more solute segregation. A similar phenomenon was indeed observed in this study.

One-dimensional concentration profiles were obtained across GBs in as-processed ECAP and HPT KD. In the concentration profiles obtained from HPT KD shown in Figure 10a and 10c, the only element found to be enriched at the GB is Si. The atomic concentrations of Fe, Cr and Al are almost identical to the nominal values. In the case of ECAP KD, concentration profiles in Figure 10b and 10d suggest that Cr and Si are enriched while Fe is depleted at the GB. It is noted that the GB analyzed in this sample is at the vicinity of a $Cr_{23}C_6$ particle as shown in Figure 11a. Therefore, the Cr concentration at the GB and in the matrix is lower than the expected value of ~20 at.% (nominal composition). Thus, it is actually not certain that Cr is enriched in the GB. If the GB was not in the

proximity of the $Cr_{23}C_6$ particle, no Cr segregation may be present at GBs in ECAP KD, similar to HPT KD.

In contrast, the Si concentration at GBs (1.577 at.%) in HPT KD is higher than that in ECAP KD (0.896 at.%). The average concentration of Si in the FeCrAl matrix in ECAP KD is 0.451 at.%, whereas that in the Cr₂₃C₆ is 0.049 at.%, suggesting that Si solubility is much lower in Cr₂₃C₆ (Figure 11c). Hence, the Si concentration at the GB will not be affected by the presence of Cr₂₃C₆ in its vicinity, making the comparison of Si segregation between ECAP KD and HPT KD fair. The higher degree of Si segregation in HPT KD is consistent with what was expected and discussed previously. Despite the higher degree of solute segregation at GBs in HPT KD, HPT KD has lower thermal stability than ECAP KD. ECAP KD is found to be thermally more stable than HPT KD in spite of a lower degree of solute segregation, and that is attributed to the higher fraction of low mobility LAGBs as discussed in the previous sections.

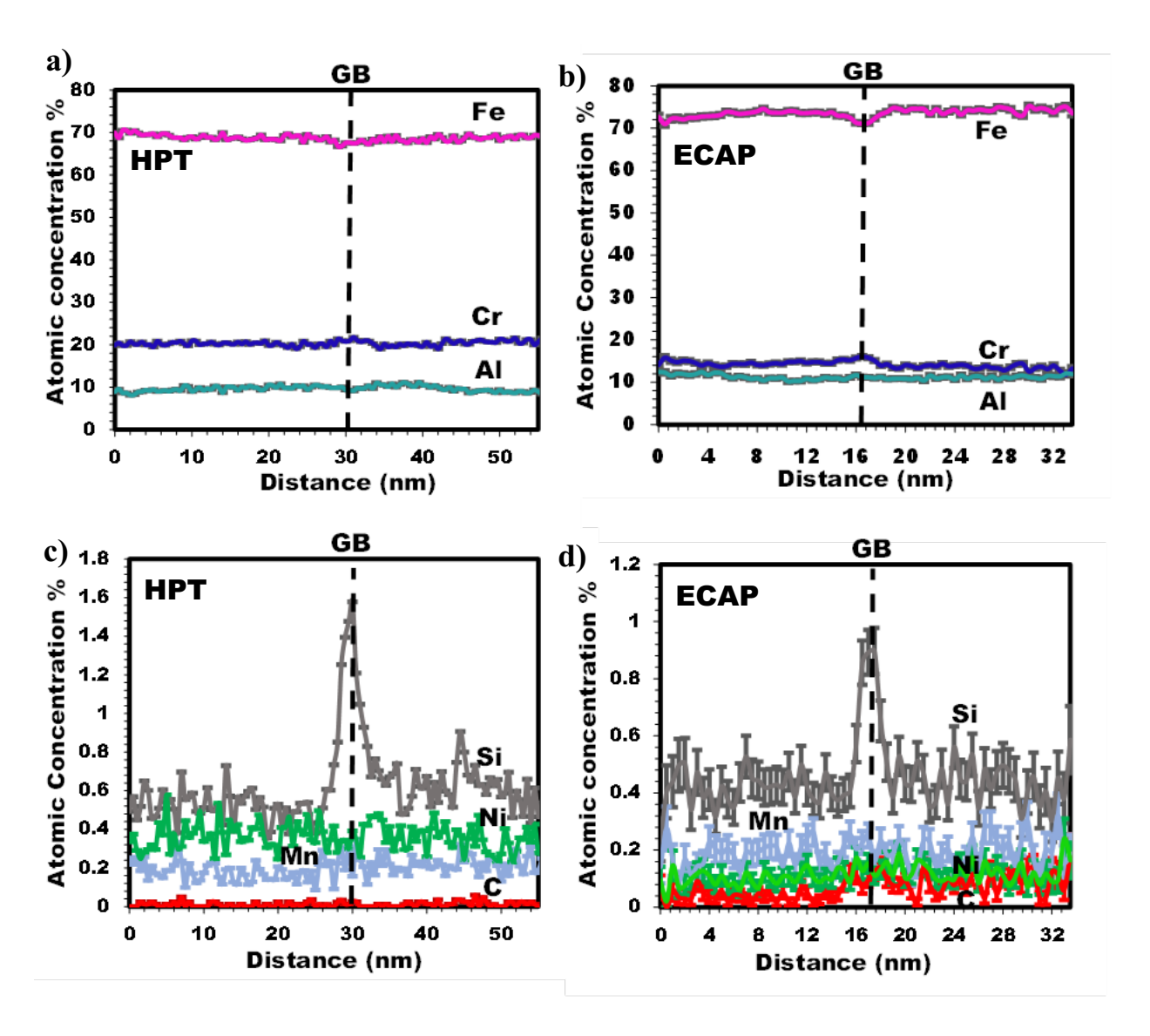


Figure 10. 1D concentration profiles from an as-processed HPT KD GB showing a) Fe, Cr and Al, and c) Si, Ni, Mn, and C. 1D concentration profiles from an ECAP KD GB showing b) Fe, Cr and Al, and d) Si, Ni, Mn, and C.

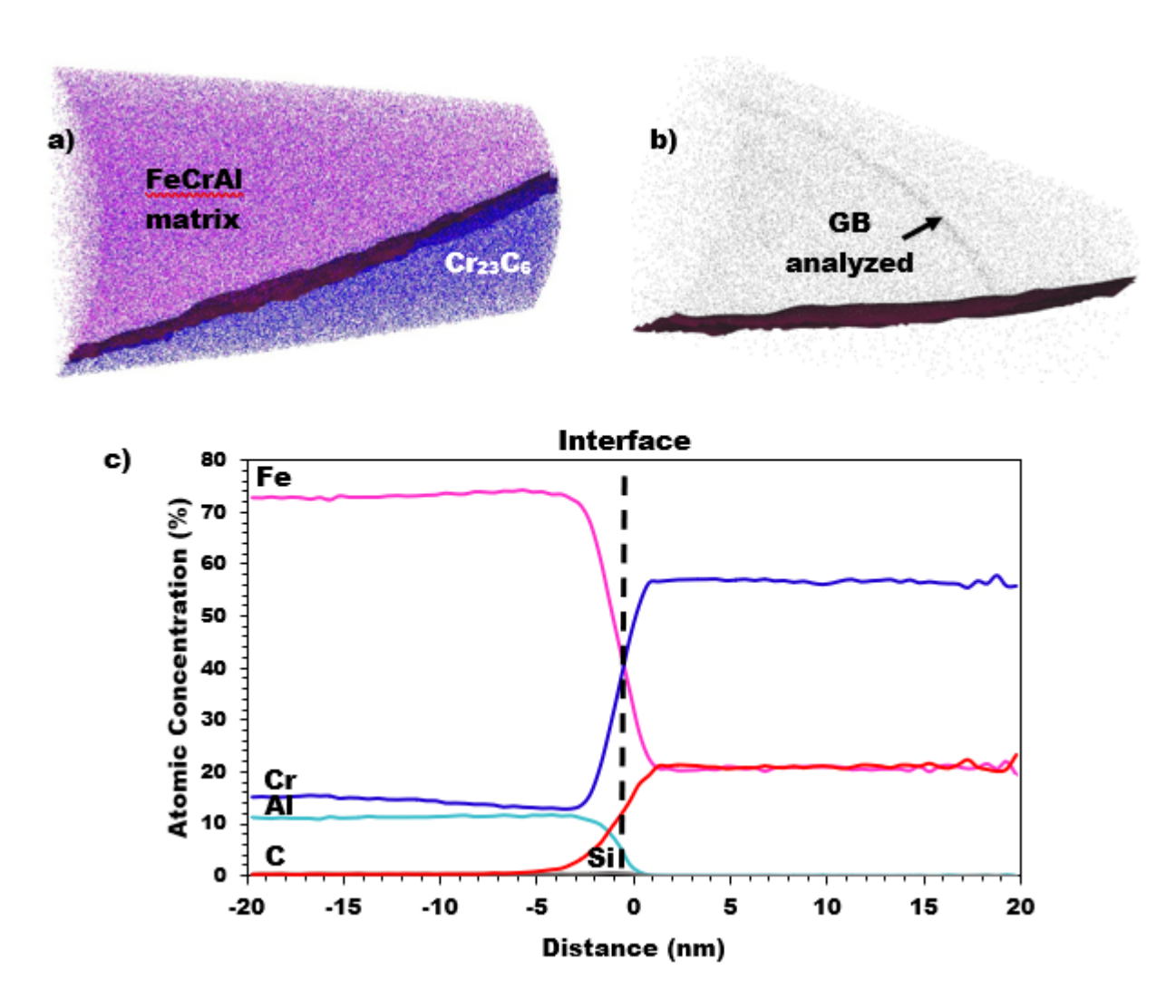


Figure 11. a) 3D APT reconstruction of ECAP KD showing Fe (pink) and Cr (blue) atoms with a 15 at.% C iso-concentration surface. b) The rotated ECAP KD APT dataset displaying Si atoms with the same 15 at.% C iso-concentration surface. c) Proximity histogram from the C iso-concentration surface shown in Figure 11a and 11b. Note that the 1D concentration profiles shown in Figure 10b and 10d were obtained from a cylinder placed across the GB indicated in Figure 11b.

 $Cr_{23}C_6$ precipitation was found to occur in the ECAP and HPT samples. Pinning of grain boundaries due to the presence of these secondary phase particles is unlikely due to the small precipitate number density [27,69–71]. Therefore, along with segregation,

precipitation is also expected to have a minor influence on the thermal stability of the SPD-processed Fe-21Cr-5Al alloys.

4.4. IMPACT OF MICROSTRUCTURAL EVOLUTION ON MECHANICAL PROPERTIES

Mechanical properties of as-processed and annealed ECAP KD was characterized using miniature tensile testing and Vickers microhardness testing, while HPT KD was investigated only using microhardness testing. The percentage elongation drops from 15.2% in CG KD to 9.2% in ECAP KD, due to increased dislocation networks and GBs impeding dislocation motion. ECAP KD annealed at 500 °C for 12h exhibits mechanical properties almost identical to those of as-processed ECAP KD, which again indicates ECAP KD is stable up to 500 °C. Nonetheless, from microstructural characterization using EBSD, ECAP KD experienced recrystallization after annealing at 600 °C for 12h. Correspondingly, Vickers microhardness measurements show a drop in hardness from 333 \pm 17 HV to 255 \pm 1 HV. This drop in hardness is attributed to the loss in dislocation strengthening and GB strengthening from recrystallization. Annealing of ECAP KD at 700 °C for 3h resulted in recrystallization, based on EBSD results. Correspondingly, a drop in tensile strength and an increase in ductility are observed for ECAP KD annealed at 700 °C for 12h (Figure 9).

5. SUMMARY AND CONCLUSIONS

Grain refinement of KD alloy was carried out using two SPD techniques of ECAP and HPT.

- i. The UTS of ECAP KD (802 MPa) was $^{\sim}1.63$ times that of CG KD (490 MPa), and average Vickers microhardness of the ECAP KD (333 \pm 17 HV) was $^{\sim}1.46$ times that of CG KD (228 \pm 4 HV), a result of dislocation strengthening and GB strengthening.
- ii. HPT KD was found to have a nanocrystalline AGS of 75 \pm 39 nm with an area fraction of HAGBs of 84.5% as estimated by TKD. Average microhardness of the HPT KD (595 \pm 11 HV) was ~2.61 times that of CG KD.
- iii. The thermal stability of ECAP KD and HPT KD was compared by annealing them at temperatures greater than 500 °C for different durations. ECAP KD was found to be stable up to 500 °C. A drop in hardness of ~80 HV (24%) from asprocessed ECAP KD was observed after annealing at 600 °C for 12h. EBSD revealed a recrystallized microstructure with a HAGB fraction of ~80%, compared to a value of ~51% in as-processed ECAP KD (determined from previous work [27]). XRD analysis of as-processed ECAP KD and annealed ECAP KD revealed a change in texture associated with recrystallization. The trend from hardness testing was consistent with that obtained from mini-tensile testing.
- iv. The hardness of HPT KD annealed at 500 °C for 3h dropped by ~180 HV in comparison to that of as-processed HPT KD. Microstructural characterization of the annealed HPT KD (including those annealed for short durations of time) indicated occurring of classic grain growth. XRD analysis of annealed HPT KD

showed no change in texture but only the narrowing of the peaks due to the removal of lattice strain and increase in crystallite size from grain growth.

From the results, it can be concluded that ECAP KD is stable up to 500 °C whereas HPT KD is not. Recrystallization occurs during annealing of ECAP KD at or above 600 °C, whereas classic grain growth governs the microstructural evolution of HPT KD during annealing at or above 500 °C. The better thermal stability of ECAP KD is attributed to a higher area fraction of less mobile LAGBs stabilizing the microstructure. The higher fraction of highly deformed HAGBs in HPT KD are prone to undergo faster GB migration, making the material thermally unstable at or above 500 °C.

ACKNOWLEDGEMENTS

This research was financially supported by U.S. Department of Energy, Office of Nuclear Energy through the NEET-NSUF (Nuclear Energy Enabling Technology – Nuclear Science User Facility) program (award number DE-NE0008524). Partial support for H. Wen came from the U.S. National Science Foundation (award number DMR-2207965). R.Z. Valiev and R.K. Islamgaliev acknowledge the Russian Science Foundation in the framework of the Project No. 22-19-00445 (RZV) and No. 22-23-00714 (RKI) for research in their part of the publication. APT research was supported by the Center for Nanophase Materials Sciences (CNMS), which is a US Department of Energy, Office of Science User

Facility at Oak Ridge National Laboratory. The authors would like to thank James Burns for assistance in performing APT sample preparation and running the APT experiments.

REFERENCES

- [1] E.O. Hall, The deformation and ageing of mild steel: II Characteristics of the Lüders deformation, Proceedings of the Physical Society. Section B. 64 (1951) 742–747. https://doi.org/10.1088/0370-1301/64/9/302.
- [2] N.J. Petch, The cleavage strength of polycrystals, Journal of Iron and Steel Institute. (1982) 25–28.
- [3] C. Sun, M. Song, K.Y. Yu, Y. Chen, M. Kirk, M. Li, H. Wang, X. Zhang, In situ
 Evidence of Defect Cluster Absorption by Grain Boundaries in Kr Ion Irradiated
 Nanocrystalline Ni, Metallurgical and Materials Transactions A. 44A (2013) 1966–
 1974. https://doi.org/10.1007/s11661-013-1635-9.
- [4] M. Song, Y.D. Wu, D. Chen, X.M. Wang, C. Sun, K.Y. Yu, Y. Chen, L. Shao, Y. Yang, K.T. Hartwig, X. Zhang, Response of equal channel angular extrusion processed ultrafine-grained T91 steel subjected to high temperature heavy ion irradiation, Acta Mater. 74 (2014) 285–295. https://doi.org/10.1016/j.actamat.2014.04.034.
- [5] Fourth Annual Report High-Temperature Materials and Reactor Component Development Programs, Cincinnati, Ohio, 1965.

- [6] J.F. Collins, F.C. Robertshaw, Advanced Long-Life Reactor Fuel Cladding and Structural Materials Development, Cincinnati, Ohio, 1967.

 https://www.osti.gov/biblio/4461970.
- [7] G.R. VanHouten, M.R. Broz, Advanced Long-Life Reactor Fuel Element,
 Moderator, Control, and Shield Materials Development, Cincinnati, Ohio, n.d.
- [8] Fifth annual report on high temperature materials programs Part A, 1966.
- [9] Seventh annual report AEC Fuels and Materials Development program, General Electric, 1968.
- [10] High-Temperature Materials Program Progress Report No. 59, Part A, GEMP-59A,1966.
- [11] High-Temperature Materials Program Progress Report No. 55, Part A, GEMP-55A,1966.
- [12] R. Valiev, Nanostructuring of metals by severe plastic deformation for advanced properties, Nat Mater. 3 (2004) 511–516. https://doi.org/10.1038/nmat1180.
- [13] Y.T. Zhu, T. G. Langdon, Z. Horita, M. J. Zehetbauer, S. L. Semiatin, T. C. Lowe,
 Ultrafine-grained materials IV, in: The Minerals, Metals, and Materials Society,
 Warrendale (PA), 2006.
- [14] I.G. Brodova, D. v Bashlykov, A.B. Manukhin, V. v Stolyarov, E.P. Soshnikova,
 Formation of nanostructure in rapidly solidified Al-Zr alloy by severe plastic
 deformation, Scr Mater. 44 (2001) 1761–1764. https://doi.org/10.1016/S1359-6462(01)00791-6.

- [15] R.Z. Valiev, R.K. Islamgaliev, I. v Alexandrov, Bulk nanostructured materials from severe plastic deformation, Prog Mater Sci. 45 (2000) 103–189.
- [16] D.C. Foley, K.T. Hartwig, S.A. Maloy, P. Hosemann, X. Zhang, Grain refinement of T91 alloy by equal channel angular pressing, Journal of Nuclear Materials. 389 (2009) 221–224. https://doi.org/10.1016/j.jnucmat.2009.02.005.
- [17] R.K. Islamgaliev, M.A. Nikitina, A.V. Ganeev, V.D. Sitdikov, Strengthening mechanisms in ultrafine-grained ferritic/martensitic steel produced by equal channel angular pressing, Materials Science and Engineering: A. 744 (2019) 163–170. https://doi.org/10.1016/j.msea.2018.11.141.
- [18] T. Müller, A. Bachmaier, A. Stark, N. Schell, R. Pippan, Nanostructured Low Carbon Steels Obtained from the Martensitic State via Severe Plastic Deformation, Precipitation, Recovery, and Recrystallization, Adv Eng Mater. 21 (2019) 1800202. https://doi.org/10.1002/adem.201800202.
- [19] D.P. Shen, H.B. Zhou, W.P. Tong, Influence of deformation temperature on the microstructure and thermal stability of HPT-consolidated Cu-1%Nb alloys, Journal of Materials Research and Technology. 8 (2019) 6396–6399. https://doi.org/10.1016/j.jmrt.2019.09.054.
- [20] A.P. Zhilyaev, B.-K. Kim, G.V. Nurislamova, M.D. Baró, J.A. Szpunar, T.G. Langdon, Orientation imaging microscopy of ultrafine-grained nickel, Scr Mater. 46 (2002) 575–580. https://doi.org/10.1016/S1359-6462(02)00018-0.

- [21] D.H. Shin, I. Kim, J. Kim, K.T. Park, Grain refinement mechanism during equal-channel angular pressing of a low-carbon steel, Acta Mater. 49 (2001) 1285–1292. https://doi.org/10.1016/S1359-6454(01)00010-6.
- [22] T. Sakai, A. Belyakov, H. Miura, Ultrafine grain formation in ferritic stainless steel during severe plastic deformation, Metall Mater Trans A Phys Metall Mater Sci. 39 (2008) 2206–2214. https://doi.org/10.1007/s11661-008-9556-8.
- [23] F. Djavanroodi, M. Ebrahimi, B. Rajabifar, S. Akramizadeh, Fatigue design factors for ECAPed materials, Materials Science and Engineering A. 528 (2010) 745–750. https://doi.org/10.1016/j.msea.2010.09.080.
- [24] A.P. Zhilyaev, T.G. Langdon, Using high-pressure torsion for metal processing: Fundamentals and applications, Prog Mater Sci. 53 (2008) 893–979. https://doi.org/10.1016/j.pmatsci.2008.03.002.
- [25] ASTM E2627-10, Standard Practice for Determining Average Grain Size Using Electron Backscatter Diffraction (EBSD) in Fully Recrystallized Polycrystalline Materials, in: ASTM International, 2013.
- [26] K. Thompson, D. Lawrence, D.J. Larson, J.D. Olson, T.F. Kelly, B. Gorman, In situ site-specific specimen preparation for atom probe tomography, Ultramicroscopy. 107 (2007) 131–139. https://doi.org/10.1016/j.ultramic.2006.06.008.
- [27] M. Arivu, A. Hoffman, J. Duan, H. Wen, R. Islamgaliev, R. Valiev, Severe plastic deformation assisted carbide precipitation in Fe-21Cr-5Al alloy, Mater Lett. 253 (2019) 78–81. https://doi.org/10.1016/j.matlet.2019.05.139.

- [28] M.S. Pham, M. Iadicola, A. Creuziger, L. Hu, A.D. Rollett, Thermally-activated constitutive model including dislocation interactions, aging and recovery for strain path dependence of solid solution strengthened alloys: Application to AA5754-O, Int J Plast. 75 (2015) 226–243.

 https://doi.org/10.1016/j.ijplas.2014.09.010.
- [29] Y. Gao, Z. Zhuang, X. You, A hierarchical dislocation-grain boundary interaction model based on 3D discrete dislocation dynamics and molecular dynamics, Sci China Phys Mech Astron. 54 (2011) 625–632. https://doi.org/10.1007/s11433-011-4298-9.
- [30] J. Kacher, B.P. Eftink, B. Cui, I.M. Robertson, Dislocation interactions with grain boundaries, Curr Opin Solid State Mater Sci. 18 (2014) 227–243. https://doi.org/10.1016/j.cossms.2014.05.004.
- [31] X. Zhang, S. Lu, B. Zhang, X. Tian, Q. Kan, G. Kang, Dislocation–grain boundary interaction-based discrete dislocation dynamics modeling and its application to bicrystals with different misorientations, Acta Mater. 202 (2021) 88–98. https://doi.org/10.1016/j.actamat.2020.10.052.
- [32] Y.C. Lin, M.S. Chen, Study of microstructural evolution during static recrystallization in a low alloy steel, J Mater Sci. 44 (2009) 835–842. https://doi.org/10.1007/s10853-008-3120-1.
- [33] A.M. Ferreira, M.A. Martorano, N.B. de Lima, A.F. Padilha, Effects of recovery and recrystallization on microstructure and texture during annealing of a cold

- deformed superconducting Nb-50(wt.)%Ti alloy, J Alloys Compd. 887 (2021) 161334. https://doi.org/10.1016/j.jallcom.2021.161334.
- [34] G.S. Rohrer, Grain boundary energy anisotropy: A review, J Mater Sci. 46 (2011) 5881–5895. https://doi.org/10.1007/s10853-011-5677-3.
- [35] R.Z. Valiev, Y. V. Ivanisenko, E.F. Rauch, B. Baudelet, Structure and deformation behaviour of Armco iron subjected to severe plastic deformation, Acta Mater. 44 (1996) 4705–4712. https://doi.org/10.1016/S1359-6454(96)00156-5.
- [36] N. Hansen, Hall-petch relation and boundary strengthening, Scr Mater. 51 (2004) 801–806. https://doi.org/10.1016/j.scriptamat.2004.06.002.
- [37] A.R. Kilmametov, G. Vaughan, A.R. Yavari, A. LeMoulec, W.J. Botta, R.Z. Valiev, Microstructure evolution in copper under severe plastic deformation detected by in situ X-ray diffraction using monochromatic synchrotron light, Materials Science and Engineering A. 503 (2009) 10–13. https://doi.org/10.1016/j.msea.2008.11.023.
- [38] M. Dao, L. Lu, R.J. Asaro, J.T.M. De Hosson, E. Ma, Toward a quantitative understanding of mechanical behavior of nanocrystalline metals, Acta Mater. 55 (2007) 4041–4065. https://doi.org/10.1016/j.actamat.2007.01.038.
- [39] X. Zhang, K. Hattar, Y. Chen, L. Shao, J. Li, C. Sun, K. Yu, N. Li, M.L. Taheri, H. Wang, J. Wang, M. Nastasi, Radiation damage in nanostructured materials, Prog Mater Sci. 96 (2018) 217–321. https://doi.org/10.1016/j.pmatsci.2018.03.002.

- [40] G.S. Rohrer, Influence of interface anisotropy on grain growth and coarsening,Annu Rev Mater Res. 35 (2005) 99–126.https://doi.org/10.1146/annurev.matsci.33.041002.094657.
- [41] L. Li, M. Saber, W. Xu, Y. Zhu, C.C. Koch, R.O. Scattergood, High-temperature grain size stabilization of nanocrystalline Fe–Cr alloys with Hf additions, Materials Science and Engineering: A. 613 (2014) 289–295.

 https://doi.org/10.1016/j.msea.2014.06.099.
- [42] F. Abdeljawad, S.M. Foiles, Stabilization of nanocrystalline alloys via grain boundary segregation: A diffuse interface model, Acta Mater. 101 (2015) 159–171. https://doi.org/10.1016/j.actamat.2015.07.058.
- [43] A.E. Perrin, C.A. Schuh, Stabilized Nanocrystalline Alloys: The Intersection of Grain Boundary Segregation with Processing Science, Annu Rev Mater Res. 51 (2021) 241–268. https://doi.org/10.1146/annurev-matsci-080819-121823.
- [44] N. Wang, Y. Ji, Y. Wang, Y. Wen, L.-Q. Chen, Two modes of grain boundary pinning by coherent precipitates, Acta Mater. 135 (2017) 226–232. https://doi.org/10.1016/j.actamat.2017.06.031.
- [45] J. Moon, C. Lee, Pinning efficiency of austenite grain boundary by a cubic shaped TiN particle in hot rolled HSLA steel, Mater Charact. 73 (2012) 31–36. https://doi.org/10.1016/j.matchar.2012.07.003.
- [46] C.J. O'Brien, C.M. Barr, P.M. Price, K. Hattar, S.M. Foiles, Grain boundary phase transformations in PtAu and relevance to thermal stabilization of bulk

- nanocrystalline metals, J Mater Sci. 53 (2018) 2911–2927. https://doi.org/10.1007/s10853-017-1706-1.
- [47] A. Hoffman, M. Arivu, H. Wen, L. He, K. Sridharan, X. Wang, W. Xiong, X. Liu, L. He, Y. Wu, Enhanced Resistance to Irradiation Induced Ferritic Transformation in Nanostructured Austenitic Steels, Materialia (Oxf). 13 (2020) 100806. https://doi.org/10.1016/j.mtla.2020.100806.
- [48] A.D. Rollett, G. Gottstein, L.S. Shvindlerman, D.A. Molodov, Grain boundary mobility A brief review, Zeitschrift Fuer Metallkunde/Materials Research and Advanced Techniques. 95 (2004) 226–229. https://doi.org/10.3139/146.017938.
- [49] U. Essmann, H. Mughrabi, Annihilation of dislocations during tensile and cyclic deformation and limits of dislocation densities, Philosophical Magazine A. 40 (1979) 731–756. https://doi.org/10.1080/01418617908234871.
- [50] M. Winning, A.D. Rollett, G. Gottstein, D.J. Srolovitz, A. Lim, L.S. Shvindlerman, Mobility of low-angle grain boundaries in pure metals, Philosophical Magazine. 90 (2010) 3107–3128. https://doi.org/10.1080/14786435.2010.481272.
- [51] G.E. Lloyd, A.B. Farmer, D. Mainprice, Misorientation analysis and the formation and orientation of subgrain and grain boundaries, Tectonophysics. 279 (1997) 55–78. https://doi.org/10.1016/S0040-1951(97)00115-7.
- [52] Y. Huang, F.J. Humphreys, Subgrain growth and low angle boundary mobility in aluminium crystals of orientation $\{110\}$ $\langle001\rangle$, Acta Mater. 48 (2000) 2017–2030. https://doi.org/10.1016/S1359-6454(99)00418-8.

- [53] M. Winning, G. Gottstein, L.S. Shvindlerman, Stress induced grain boundary motion, Acta Mater. 49 (2001) 211–219. https://doi.org/10.1016/S1359-6454(00)00321-9.
- [54] M. Winning, Motion of $\langle 1\,0\,0 \rangle$ -tilt grain boundaries, Acta Mater. 51 (2003) 6465–6475. https://doi.org/10.1016/j.actamat.2003.06.001.
- [55] D. MOLODOV, V. IVANOV, G. GOTTSTEIN, Low angle tilt boundary migration coupled to shear deformation, Acta Mater. 55 (2007) 1843–1848. https://doi.org/10.1016/j.actamat.2006.10.045.
- [56] R. Viswanathan, C.L. Bauer, Kinetics of grain boundary migration in copper bicrystals with [001] rotation axes, Acta Metallurgica. 21 (1973) 1099–1109. https://doi.org/10.1016/0001-6160(73)90026-6.
- [57] M. Winning, A.D. Rollett, G. Gottstein, D.J. Srolovitz, A. Lim, L.S. Shvindlerman, Mobility of low-angle grain boundaries in pure metals, Philosophical Magazine. 90 (2010) 3107–3128. https://doi.org/10.1080/14786435.2010.481272.
- [58] M.J. Rahman, H.S. Zurob, J.J. Hoyt, A comprehensive molecular dynamics study of low-angle grain boundary mobility in a pure aluminum system, Acta Mater. 74 (2014) 39–48. https://doi.org/10.1016/j.actamat.2014.03.063.
- [59] Z. Nasiri, S. Ghaemifar, M. Naghizadeh, H. Mirzadeh, Thermal Mechanisms of Grain Refinement in Steels: A Review, Metals and Materials International. 27 (2021) 2078–2094. https://doi.org/10.1007/s12540-020-00700-1.

- [60] G.J. Tucker, D.L. McDowell, Non-equilibrium grain boundary structure and inelastic deformation using atomistic simulations, Int J Plast. 27 (2011) 841–857. https://doi.org/10.1016/j.ijplas.2010.09.011.
- [61] A. Hasnaoui, H. Van Swygenhoven, P.M. Derlet, On non-equilibrium grain boundaries and their effect on thermal and mechanical behaviour: a molecular dynamics computer simulation, Acta Mater. 50 (2002) 3927–3939.

 https://doi.org/10.1016/S1359-6454(02)00195-7.
- [62] H.E. Vatne, T. Furu, R. Ørsund, E. Nes, Modelling recrystallization after hot deformation of aluminium, Acta Mater. 44 (1996) 4463–4473. https://doi.org/10.1016/1359-6454(96)00078-X.
- [63] F.J. Humphreys, A unified theory of recovery, recrystallization and grain growth, based on the stability and growth of cellular microstructures—I. The basic model, Acta Mater. 45 (1997) 4231–4240. https://doi.org/10.1016/S1359-6454(97)00070-0.
- [64] P.J. Hurley, F.J. Humphreys, Modelling the recrystallization of single-phase aluminium, Acta Mater. 51 (2003) 3779–3793. https://doi.org/10.1016/S1359-6454(03)00192-7.
- [65] H. ZUROB, Y. BRECHET, J. DUNLOP, Quantitative criterion for recrystallization nucleation in single-phase alloys: Prediction of critical strains and incubation times, Acta Mater. 54 (2006) 3983–3990. https://doi.org/10.1016/j.actamat.2006.04.028.

- [66] M. Herbig, D. Raabe, Y.J. Li, P. Choi, S. Zaefferer, S. Goto, Atomic-Scale

 Quantification of Grain Boundary Segregation in Nanocrystalline Material, Phys

 Rev Lett. 112 (2014) 126103. https://doi.org/10.1103/PhysRevLett.112.126103.
- [67] X. Zhou, X. Yu, T. Kaub, R.L. Martens, G.B. Thompson, Grain Boundary Specific Segregation in Nanocrystalline Fe(Cr), Sci Rep. 6 (2016) 34642. https://doi.org/10.1038/srep34642.
- [68] J. Wang, R. Janisch, G.K.H. Madsen, R. Drautz, First-principles study of carbon segregation in bcc iron symmetrical tilt grain boundaries, Acta Mater. 115 (2016) 259–268. https://doi.org/10.1016/j.actamat.2016.04.058.
- [69] Z. Li, J. Wang, H. Huang, Influences of grain/particle interfacial energies on second-phase particle pinning grain coarsening of polycrystalline, J Alloys Compd. 818 (2020) 152848. https://doi.org/10.1016/j.jallcom.2019.152848.
- [70] F. Yan, W. Xiong, E. Faierson, Grain Structure Control of Additively Manufactured
 Metallic Materials, Materials. 10 (2017) 1260.
 https://doi.org/10.3390/ma10111260.
- [71] S. Chen, K.-K. Tseng, Y. Tong, W. Li, C.-W. Tsai, J.-W. Yeh, P.K. Liaw, Grain growth and Hall-Petch relationship in a refractory HfNbTaZrTi high-entropy alloy, J Alloys Compd. 795 (2019) 19–26. https://doi.org/10.1016/j.jallcom.2019.04.291.